ResearchGate

See discussions, stats, and author profiles for this publication at: https://www.researchgate.net/publication/233855586

An experimental study on turbulence modification in the near-wall boundary layer of a dilute gas-particle channel flow

ARTICLE *in* EXPERIMENTS IN FLUIDS · NOVEMBER 2012

Impact Factor: 1.67 · DOI: 10.1007/s00348-012-1364-7

CITATIONS
4

READS
69

5 AUTHORS, INCLUDING:

Jing Li
Huazhong University of Science and Techn…

9 PUBLICATIONS **48** CITATIONS

SEE PROFILE

Hanfeng Wang
Central South University

19 PUBLICATIONS **158** CITATIONS

SEE PROFILE

Zhaohui Liu
Huazhong University of Science and Techn…

93 PUBLICATIONS **614** CITATIONS

SEE PROFILE

All in-text references underlined in blue are linked to publications on ResearchGate, letting you access and read them immediately.

Available from: Zhaohui Liu
Retrieved on: 23 January 2016

Exp Fluids (2012) 53:1385–1403
DOI 10.1007/s00348-012-1364-7

RESEARCH ARTICLE

An experimental study on turbulence modification in the near-wall boundary layer of a dilute gas-particle channel flow

Jing Li · Hanfeng Wang · Zhaohui Liu · Sheng Chen · Chuguang Zheng

Received: 19 March 2012 / Revised: 7 August 2012 / Accepted: 9 August 2012 / Published online: 30 August 2012
© Springer-Verlag 2012

Abstract Turbulence modifications of a dilute gas-particle flow are experimentally investigated in the lower boundary layer of a horizontal channel by means of a simultaneous two-phase PIV measurement technique. The measurements are conducted in the near-wall region with $y^+ < 250$ at Re_τ (based on the wall friction velocity u_τ and half channel height h) = 430. High spatial resolution and small interrogation window are used to minimize the PIV measurement uncertainty due to the velocity gradient near the wall. Polythene beads with the diameter of 60 μm ($d_p^+ = 1.71$, normalized by the fluid kinematic viscosity ν and u_τ) are used as dispersed phase, and three low mass loading ratios (Φ_m) ranging from 10^{-4} to 10^{-3} are tested. It is found that the addition of the particles noticeably modifies the mean velocity and turbulent intensities of the gas-phase, as well as the turbulence coherent structures, even at $\Phi_m = 0.025$ %. Particle inertia changes the viscous sublayer of the gas turbulence with a smaller thickness and a larger streamwise velocity gradient, which increases the peak value of the streamwise fluctuation velocity (u_{rms}^+) of the gas-phase with its location shifting to the wall. Particle sedimentation increases the roughness of the bottom wall, which significantly increases the wall-normal fluctuation velocity (v_{rms}^+) and Reynolds shear stress ($-\langle u'v'\rangle^+$) of the gas-phase in the inner region of the boundary layer ($y^+ < 10$). Under effect of particle–wall collision, the Q2 events (ejections) of the gas-phase are slightly increased by particles, while the Q4 events (sweeps) are obviously decreased. The spatial scale of the coherent structures near the wall shrinks remarkably with the presence of the particles, which may be attributed to the intensified crossing-trajectory effects due to particle saltation near the bottom wall. Meanwhile, the v_{rms}^+ and $-\langle u'v'\rangle^+$ of the gas-phase are significantly reduced in the outer region of the boundary layer ($y^+ > 20$).

J. Li · Z. Liu (✉) · S. Chen · C. Zheng
State Key Laboratory of Coal Combustion,
Huazhong University of Science and Technology,
Wuhan 430074, People's Republic of China
e-mail: zliu@hust.edu.cn

H. Wang
School of Civil Engineering, Central South University,
Changsha 410000, People's Republic of China

List of symbols

d_p	Particle diameter (m)
d_p^+	Dimensionless particle diameter (= $d_p \times u_\tau/\nu$)
g	Gravity (m × s^{-2})
h	Half channel height (m)
l_e	Characteristic length scale of energy-containing eddies (m)
PIV	Particle image velocimetry
PTV	Particle-tracking velocimetry
Re_b	Reynolds number based on time-averaged bulk velocity (= $U_b \times h/\nu$)
Re_p	Particle Reynolds number (= $u_R \times d_p/\nu$)
Re_τ	Reynolds number based on the wall friction velocity (= $u_\tau \times h/\nu$)
$\mathrm{R_{uu}}$	Spatial two-point correlation coefficients of streamwise velocity component
$\mathrm{R_{vv}}$	Spatial two-point correlation coefficients of wall-normal velocity component
S	Density ratio (= ρ_p/ρ_f)
St	Stokes number based on the particle relaxation time and the characteristic time scale of energy-containing eddy (= τ_p/τ_e)
St_b	Bulk Stokes number (= $\tau_p \times U_{cl}/h$)
St_w	Wall Stokes number (= $\tau_p \times u_\tau^2/\nu$)

TKE	Turbulence kinetic energy
u_f	Fluid velocity (m × s^{-1})
u_p	Particle velocity (m × s^{-1})
u_R	Relative velocity between the particle and surrounding fluid (m × s^{-1})
u_τ	Wall friction velocity (m × s^{-1})
u^+_{rms}	Dimensionless streamwise r.m.s. velocity of the fluid
$-\langle u'v'\rangle^+$	Dimensionless Reynolds shear stress
U_{cl}	Fluid centreline velocity (m × s^{-1})
U_b	Fluid time-averaged bulk velocity (m × s^{-1})
U^+	Dimensionless streamwise mean velocity of the fluid
v^+_{rms}	Dimensionless wall-normal r.m.s. velocity of the fluid
V_s	Particle settling velocity (m × s^{-1})
x	Cartesian coordinate in the streamwise direction (m)
x^+	Dimensionless coordinate in the streamwise direction
y	Cartesian coordinate in wall-normal direction (distance from the bottom wall) (m)
y^+	Dimensionless distance from the wall (= $y \times u_\tau/\nu$)
ν	Fluid kinematic viscosity (m^2 × s^{-1})
ρ_f	Fluid density (kg × m^{-3})
ρ_p	Particle density (kg × m^{-3})
σ	Standard deviation for the particle diameter (μm)
τ_e	Characteristic time scale of energy-containing eddies (ms)
τ_f	Fluid response time (ms)
τ_p	Particle relaxation time (ms)
τ_p^+	Dimensionless particle relaxation time (= $\tau_p \times u_\tau^2/\nu$)
τ_v	Viscous response time ($d^2S/18\nu$) (ms)
Φ_m	Averaged particle mass loading ratio
Φ_v	Averaged particle volume fraction

1 Introduction

Turbulent particle-laden flows are frequently encountered in the natural environment and industrial processes, such as sandstorm, fluidized bed and pneumatic conveying of solid particles. The interaction between particles and turbulent flow is complex, as there are many parameters involved, for example, particle mass loading ratio Φ_m (Tsuji and Morikawa 1982), particle Reynolds number Re_p (Hetsroni 1989), particle Stokes number St (Kulick et al. 1994), gravity g (Elghobashi and Truesdell 1993), inter-particle spacing (Sato et al. 2000), wall roughness (Kussin and Sommerfeld 2002) and velocity gradient of the flow (Li et al. 2010a). Based on the particle volume fraction (Φ_v), the interaction between particles and turbulence can be divided into three regimes (Elghobashi 1994). When $\Phi_v \leq 10^{-6}$, particles are carried by fluid and their effects on the fluid turbulence is negligibly small. The interaction in this regime is named one-way coupling. When $10^{-6} < \Phi_v \leq 10^{-3}$, the momentum transferred from particles to fluid is large enough to modify the turbulence properties, and the interaction in this regime is called two-way coupling. For $\Phi_v > 10^{-3}$, inter-particle collisions occur and have significant effect on fluid turbulence. This regime is characterized by four-way coupling. Generally, flows with $\Phi_v < 10^{-3}$ or $>10^{-3}$ are referred to as dilute or dense suspensions, respectively.

With sufficient mass loading ratio, corresponding Φ_v ranges from 10^{-4} to 10^{-2}, the presence of the particles can dramatically modify the fluid turbulence, that is, enhancing or suppressing the turbulence intensity (Tsuji and Morikawa 1982; Tsuji et al. 1984; Sun and Faeth 1986; Liljegren and Vlachos 1990; Parthasarathy and Faeth 1990; Rogers and Eaton 1991; Kulick et al. 1994; Kussin and Sommerfeld 2002; Righetti and Romano 2004). Several criterions were proposed to predict the turbulence modulation caused by particles. Gore and Crowe (1989) reviewed the data measured at the centreline of pipe flow and free jet and found the ratio of d_p/l_e, where d_p is the particle diameter and l_e is the characteristic length scale of energy-containing eddies, can be used as a criterion to determine the turbulence modification. Particles with $d_p/l_e > 0.1$ enhance turbulence, while those with $d_p/l_e < 0.1$ suppress it. Hetsroni (1989) suggested Re_p ($\equiv u_R \times d_p/\nu$,where $u_R = u_f - u_p$ is the slip velocity between particle and fluid, and ν is the kinematic viscosity of fluid) may also be used as a criterion. He concluded that particles with $Re_p > 400$ enhance the turbulence owing to the vortex shedding downstream the particles, while particles with $Re_p < 400$ suppress turbulence by acting as an additional source of dissipation. By comparing the experimental data of homogeneous flow and wall-bounded flow, Eaton (1994) found the turbulence modulation is also related to Φ_m, St ($\equiv \tau_p/\tau_e$, in which τ_p is the particle relaxation time and τ_e is the characteristic time scale of energy-containing eddies) and changes in the flow structure caused by preferential particle concentration.

Several recent experiments in horizontal channel (Tanière et al. 1997; Kaftori et al. 1998; Kiger and Pan 2002; Wu et al. 2006; Li et al. 2010b) revealed that, even for $0.72 \times 10^{-6} < \Phi_v < 2.3 \times 10^{-4}$ (which belongs or is close to the one-way coupling regime), the presence of the particles still results in a significant turbulence modulation. Table 1 lists the related parameters for these investigations. It is worth mentioning that a noticeable turbulence

Table 1 Selected prior studies on liquid–solid/gas–solid horizontal channel flows

Study	Fluid	Density ratio $S = \rho_p/\rho_f$	Mass fraction Φ_m ($\times 10^{-2}$)	Volume fraction Φ_v ($\times 10^{-4}$)
Tanière et al. (1997)	Air	2,100 (glass)	1.05	0.05
		1,200 (PVC)	0.6	0.05
Kaftori et al. (1998)	Water	1.03	0.01–0.02	0.95–1.9
Kiger and Pan (2002)	Water	2.6	0.06	2.3
Wu et al. (2006)	Air	877	0.06–4	0.0072–0.48
Li et al. (2010b)	Air	877	0.1–0.5	0.012–0.06

modification was observed away from the bottom wall of the horizontal channel (Tanière et al. 1997, Wu et al. 2006), although the local Φ_v may be much smaller than 1×10^{-6}, since most particles concentrate near the bottom wall under the effect of gravity. The distortion of turbulence structure in the boundary layer caused by the particles may be an important factor to explain this phenomenon. A similar view also has been mentioned by Eaton (1995).

The near-wall turbulent flow is dominated by the coherent structures, characterized by alternating narrow streaks of high- and low-streamwise velocity and quasi-streamwise vortices (Kline et al. 1967; Cantwell 1981; Smith and Metzler 1983; Hussain 1986; Robinson 1991). These near-wall structures interact intermittently with the outer flow through strong quasi-periodic events, including both ejections of low-speed fluid from the wall (Q2 events) and sweeps of high-speed fluid towards the wall (Q4 events) (Robinson 1991). Both ejections and sweeps are the major sources of Reynolds shear stress and play key roles in the self-sustaining mechanism of turbulence (Kim et al. 1971; Lu and Willmarth 1973; Sheng et al. 2009). The ejections, also referred to as 'bursting' (Robinson 1991), dominate the turbulence kinetic energy (TKE) production and transport at $y^+ > 12$, while sweeps dominate the near-wall region, that is, $y^+ < 12$ (Willmarth and Lu 1972; Brodkey et al. 1974; Kim et al. 1987; Wallace 2009). The superscript '+' indicates wall-unit distances, normalized by the wall friction velocity (u_τ) and ν.

A number of experimental and numerical investigations (Owen 1969; Sumer and Oguz 1978; Sumer and Deigaard 1981; Brooke et al. 1992; Pedinotti et al. 1992; Kaftori et al. 1995; Rouson and Eaton 2001; Kiger and Pan 2002; Marchioli and Soldati 2002; Hout 2011) have shown that sweeps are responsible for particle deposition, while ejections tend to transfer particles from the near-wall region to the outer flow. Under the effect of streaky structures, particles with $\rho_p/\rho_f > 1$ (where ρ is the density, the subscripts p and f denote particle and fluid, respectively) tend to accumulate in low-speed, low-vorticity and high-strain-rate regions, especially for the particles with $\tau_p^+ < 3$ (Pedinotti et al. 1992).

However, information about the effect of particles on the coherent structures near a wall is relatively limited. Rashidi et al. (1990) conducted experiments for liquid-particle turbulent flow in an open channel and found the presence of the particles with $\rho_p/\rho_f = 1.03$ and $d_p = 1{,}100$ μm ($d_p^+ \approx 12$) increases the occurrence of wall ejections, as well as the Reynolds shear stress and TKE, even at $\Phi_v \approx 10^{-4}$, while small particles with $d_p = 120$ μm ($d_p^+ \approx 1.3$) reduce the occurrence of wall ejections. With Laser Doppler Anemometry (LDA) and flow visualization techniques, Kaftori et al. (1998) studied the effect of particles on wall turbulence. They found that polystyrene particles with $\rho_p/\rho_f = 1.03$ and $d_p^+ = 1$–18 reduce the occurrence frequency of the coherent structures near the wall. This reduction was found to be proportional to d_p and Φ_v. Based on DNS results, Pan and Banerjee (1996) investigated the turbulence modulation in a horizontal open channel for Φ_v ranges from 2×10^{-4} to 5×10^{-4}. They found that the particles with small density ratio ($\rho_p/\rho_f = 1.05$) can modify both ejections and sweeps and their influence on the latter is more remarkable than on the former. Their DNS results also suggested that the small particles ($d_p^+ \approx 1$) reduce the frequency of sweeps, whereas the large particles ($d_p^+ \approx 4$) apparently increase it.

Obviously, the mechanism of turbulence modulation caused by the particles with high density ratio ($\rho_p/\rho_f \gg 1.0$) is distinct from that with low density ratio ($\rho_p/\rho_f \approx 1.0$), especially in a horizontal channel. Particles with $\rho_p/\rho_f \gg 1.0$ are characterized by the saltation near the bottom wall (Ciccone et al. 1990; Sommerfeld 2003; Tanière et al. 1997), while those with $\rho_p/\rho_f \approx 1.0$ tend to suspend in the whole flow region (Kaftori et al. 1995; Kiger and Pan 2002; Hout 2011). Dritselis and Vlachos (2008) investigated the effect of particles with $\rho_p/\rho_f = 7{,}333$ and $\tau_p^+ = 200$ (copper bead in air) on the turbulent coherent structures in a vertical channel. They suggested that the copper beads with $d_p^+ = 0.7$ and $\Phi_v = 6.8 \times 10^{-5}$ suppress the strength of the coherent structures, but elongate their streamwise extent relative to those of the single-phase flow.

Besides the above-mentioned investigations, the effects of particles with high density ratio on the turbulence

modulation and coherent structures are not thoroughly understood, especially for a dilute two-phase horizontal flow. The aim of this work is to study the turbulence modulation and the variation of the coherent structures caused by particles with $\rho_p/\rho_f = 877$ (polythene beads in air), in a fully developed horizontal channel at three low Φ_m, that is, 0.025 %, 0.1 % and 0.5 %. A two-phase particle image velocimetry (PIV) technique was utilized to measure the velocities for both air flow and particles simultaneously. Based on the experimental results, qualitative information about the turbulent modulation was provided and the variation of the coherent structures was also addressed in the context of spatial two-point correlation and quadrant analysis.

2 Experimental details

2.1 Experimental set-up and PIV measurements

The experiments were conducted in a horizontal channel, as shown in Fig. 1. The height (2 h), width and length of the channel are 3, 30 and 600 cm, respectively. The length-to-height ratio of the channel is 200, ensuring the flow fully developed in the test section (Eckelmann 1974). The test section of the channel was made of glass to allow PIV measurements.

The PIV measurements were conducted in the central symmetry (x, y)-plane near the bottom wall of the test section. The flow was seeded by smoke generated from mineral oil. The averaged seeding particle diameter was about 5 μm. Flow illumination was provided by two New Wave standard pulse laser sources of 532 nm wavelength, each with a maximum energy output of 120 mJ/pulse. The thickness of the laser sheet in the measurement area was about 0.5 mm. Each laser pulse lasted for 0.01 μs. Particle images were taken at the frequency of 3.75 Hz, using one CCD camera (PIVCAM 13-8 8-bit CCD 1,280 × 1,024 pixels), in conjunction with a Nikon PK-13 auto extension ring and a 105-mm Micro-Nikkor lens. Synchronization between image taking and flow illumination was provided by a Synchronizer (Model 610034, TSI). The spatial resolution was 7.785 μm/pixel, so that the total measurement area covered about 9.96 × 7.97 mm^2, corresponding to 284 × 227 in wall units.

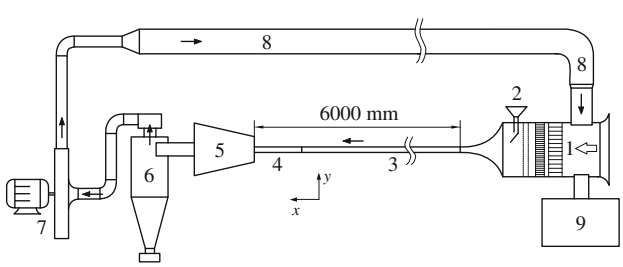

Fig. 1 Schematic diagram of experimental set-up: *1* honeycomb section, *2* particle feeder, *3* development section, *4* test section, *5* stabilization tank, *6* cyclone, *7* blower, *8* tracers recycle pipe, *9* tracer generator

For the single-phase flow, a cross-correlation method was used to get the velocity vectors. An interrogation window of 32 × 16 pixels was used with 50 % overlap in the x direction, which provides total 4977 vectors in one frame. The actual size of the interrogation area was 0.250 mm × 0.125 mm in the streamwise and wall-normal directions, corresponding to 7.10 × 3.55 in wall units. Liu et al. (1991) found that the precision of PIV with sufficient resolution (7.5 × 2.25 in wall units) was similar to that of LDA, which ensures enough precision for the present measurements.

2.2 Image processing and PTV techniques

For the gas-particle two-phase flow, the captured raw pictures contain the images of both solid particles and tracers, as shown in Fig. 2a. The arrow in Fig. 2a indicates a typical particle image. Generally, the particle image is larger in size and has higher level of brightness relative to that of the tracer. In order to get the velocities for particles and gas-phase, respectively, the particle images must be separated from the raw pictures. The image processing technique used presently is similar to that proposed by Khalitov and Longmire (2002). Briefly, the raw pictures are first filtered using Gaussian blur to reduce high-frequency spatial noise. Figure 2b shows the processed picture that contains the filtered images of both tracers and particles. Then, both brightness and size thresholds are used to separate the images of tracers and particles, as shown in Fig. 2c, d. These thresholds are chosen to ensure only the particle images with larger size and higher brightness can be detected. About 5 % randomly selected pictures of the separated particles were compared visually with the raw pictures to ensure the present image processing technique worked properly.

The pictures of the separated tracers can be analysed using cross-correlation method, similar to that used for the single-phase flow, as described in Sect. 2.1. While for the pictures of separated solid particles, a PTV (particle-tracking velocimetry) algorithm (Kazuo and Hang-Yu 2000) was used to calculate the velocity vector for each of the detected solid particles. The velocity field for the gas-phase and the velocity vectors for the detected particles are shown in Fig. 2e, f.

2.3 Experimental conditions

For the single-phase flow, the time-averaged bulk velocity (U_b) in the test section was 6.64 ± 0.08 m/s,

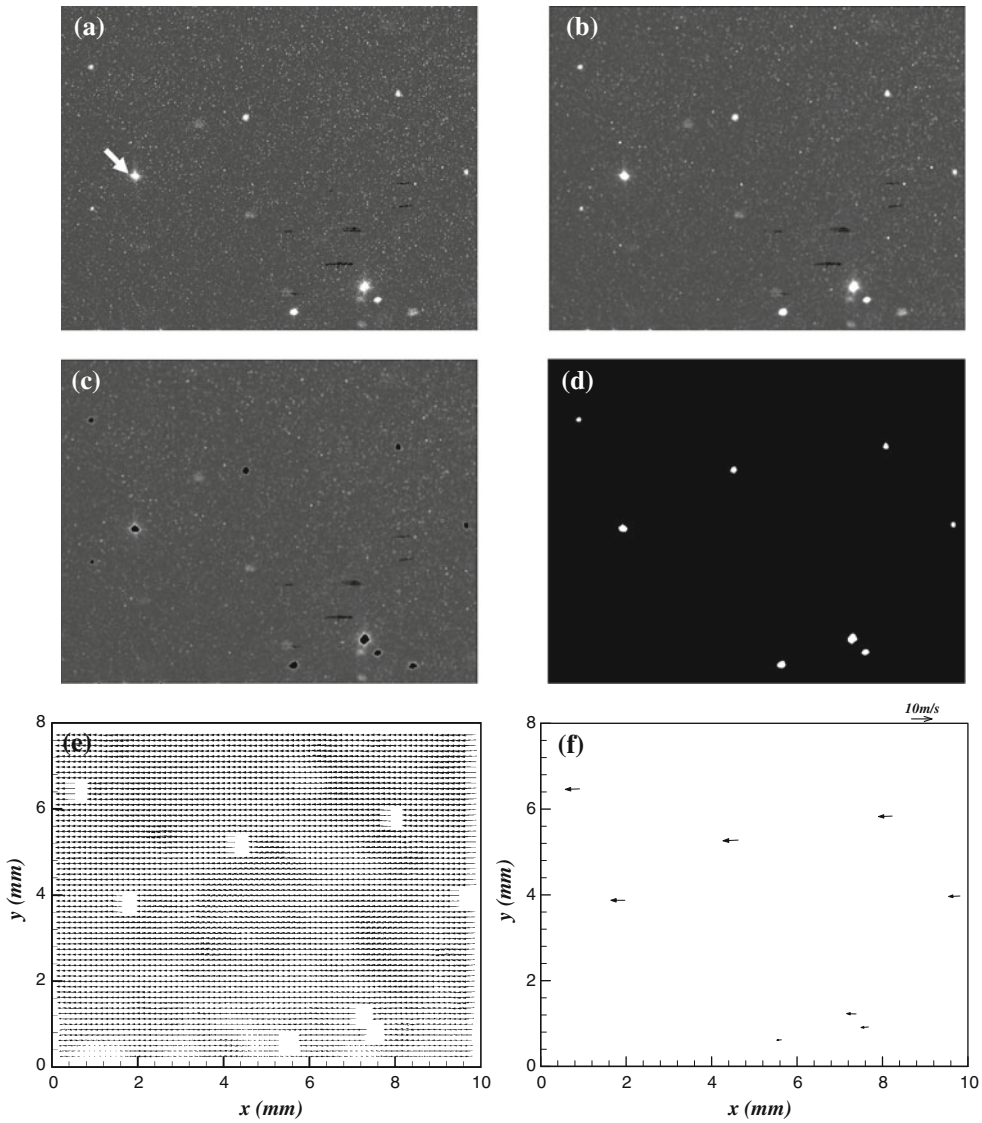

Fig. 2 Image processing procedures: **a** raw image, **b** filtered image, **c** image of separated tracer, **d** image of separated solid particles, **e** vector field of gas velocity, **f** vector field of solid particles

corresponding to a Reynolds number Re_b ($\equiv U_b \times h/\nu$) of about 6385. Based on the method proposed by Hagiwara et al. (2002), the wall friction velocity (u_τ) was estimated to be 0.445 ± 0.005 m/s, corresponding to a wall Reynolds number Re_τ ($\equiv u_\tau \times h/\nu$) of about 430.

For the gas-particle two-phase flow, polythene particles with average diameter of 60 μm (standard deviation of 4.8 μm) were added into the flow by a powder feeder located upstream to the contraction section (see Fig. 1). The particles were removed from the flow by a cyclone before entering into the blower. The material density of polythene is 1,030 kg/m^3, corresponding to a ρ_p/ρ_f of 877. Three mass loading ratios (Φ_m) were tested, that is, 0.025, 0.1 and 0.5 %, corresponding to the averaged Φ_v of 2.85×10^{-7}, 1.15×10^{-6} and 5.75×10^{-6}. During the experiments for the two-phase flow, the input power of the blower was kept the same as that for the single-phase flow. The related parameters of experimental conditions are summarized in Table 2. Note that, the slip velocity u_R ($= u_f - u_p$) in present paper was calculated based on the local velocity difference between the gas and solid particle, similar to that used in Kiger and Pan (2002). The u_p was determined by the PTV method, as mentioned in Sect. 2.2, while the u_f at the same point was determined by means of bicubic interpolation with 16 nearest-neighbour velocities. The particle Reynolds number is therefore more accurate than that based on the time-averaged slip velocity.

2.4 Statistical method for gas and particle properties

The average property of the carrier phase was generated by taking the mean over the homogeneous (streamwise) direction and over all instantaneous realizations in the ensemble. The expression for the mean of a spatially and temporally discretized variable is given by

Table 2 Flow conditions and particle properties

Fluid density, ρ_f (kg × m^{-3})	1.175
Kinematic viscosity, ν (m^2 × s^{-1})	1.56 × 10^{-5}
Fluid centreline velocity, U_{cl} (m × s^{-1})	8.85 ± 0.09
Fluid time-averaged bulk velocity, U_b (m × s^{-1})	6.64 ± 0.08
Fluid friction velocity, u_τ (m × s^{-1})	0.445 ± 0.005 (particle-free)
Fluid response time, $\tau_f = \nu/u_\tau^2$ (ms)	7.89 × 10^{-2}
Channel half height, h (m)	0.015
Mass loading ratio, Φ_m (%)	0.025, 0.1, 0.5
Particle density, ρ_p (kg × m^{-3})	1,030
Mean diameter, d_p (μm)	60
Nondimensional, $d_p^+ = d_p u_\tau/\nu$	1.71
Size range (min–max) (μm)	53–74
Standard deviation for the diameter, σ (μm)	4.8
Location slip velocity (max), max $(u_f - u_p)$ (m × s^{-1})	1–1.16
Particle Reynolds number (max), $Re_p = (u_f - u_p)_{\max} d_p/\nu$	3.83–4.46
Viscous response time, $\tau_v = d_p^2 S/18\nu$ (ms)	11.2
Corrected particle response time, τ_p (ms)	7.90–8.15
Corrected particle settling velocity, V_s (m × s^{-1})	0.077–0.08
Bulk Stokes number, $St_b = \tau_p\, U_{cl}/h$	4.66–4.80
Wall Stokes number, $St_w = \tau_p\, u_\tau^2/\nu$	100.2–103.3

$$\overline{\psi}_f(y_i) = \Psi_f(y_i) = \frac{1}{N_x(y_i) \times N_e} \sum_{j=1}^{N_x} \sum_{k=1}^{N_e} \psi_f(x_j, y_i, k) = \frac{1}{N_f(y_i)} \sum_{l=1}^{N_f} \psi_{f,l} \quad (1)$$

where $N_x(y_i)$ is the number of samples within a box of length L in the streamwise direction and the height Δy_i at one instant in time, N_e is the number of instantaneous realizations within the ensemble, and $N_f(y_i) = N_x(y_i) \times N_e$ is the total number of samples in the ensemble. For the fluid-only moments, Δy_i corresponds to wall-normal vector spacing and is uniform throughout the region of interest.

Approximately 23,500 dispersed phase particles were tracked within the image set at the mass loading of 0.5 %, and the moments of particle properties were obtained using 19 finite-sized bins spaced non-uniformly in the wall-normal direction. This was done to maximize the number of particles with each bin, while minimizing the effect of strong gradients on the resulting quantities. The bin locations and sizes are shown in Fig. 3. The length of each bar in Fig. 3 indicates the number of particles indentified in each bin. The mean value of the particles was obtained by averaging the dispersed phase property ψ_p over all particles of the ensemble contained within the region $y_i \pm \Delta y_i/2$:

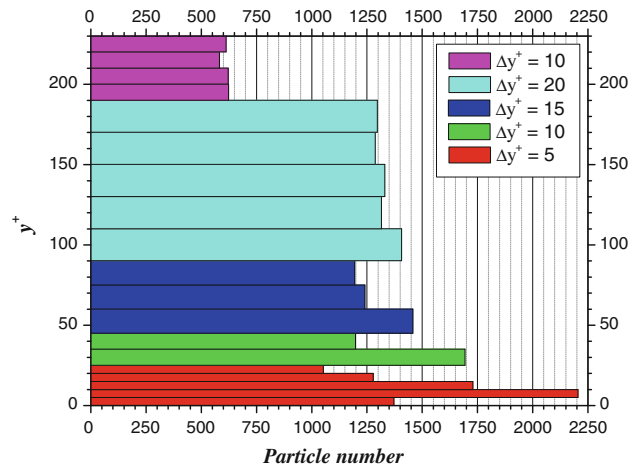

Fig. 3 Identified particles in each bin for $\Phi_m = 0.5$ %. Bin location and thickness of each bin are indicated by the *coloured bars*

$$\overline{\psi}_p(y_i) = \Psi_p(y_i) = \frac{1}{N_p(y_i)} \sum_{j=1}^{N_p} \psi_{p,j} \quad (2)$$

The fluctuation of the gas and particle properties follows the standard definition, once a mean is defined:

$$\sqrt{\overline{\widetilde{\psi}^2}} = \psi' = \sqrt{\frac{1}{N} \sum_{j=1}^{N} (\psi - \overline{\psi})^2}. \quad (3)$$

2.5 Uncertainty analysis of near-wall PIV measurement

PIV measurements consist of bias and precision (or random) uncertainties. The bias uncertainty can be reduced or even removed by careful calibration (Stern et al. 1999, Raffel et al. 2001). The precision uncertainty or random error mainly comes from PIV setting parameters, such as spatial resolution, background noise, tracer particle density, particle image size and image displacement (Raffel et al. 2001). For the near-wall PIV measurements, several issues, that is, the determination of wall position, the tracer particle density and the velocity gradient near the wall, become crucial for the measurement uncertainties (Cameron 2011). Special attention has been paid to these issues to minimize the measurement uncertainties.

Firstly, in the present experiments, the tracer particles near the wall can form clear mirror images, as shown in Fig. 4. Based on mirror imaging principle, the midpoint of the tracer particles and their mirror images can be determined as the position of wall surface. This method is similar to that used by Tsuei and Savaş (2000). The maximum uncertainty of the determined wall location is estimated to be about 1 pixels, corresponding to 0.22 in wall units.

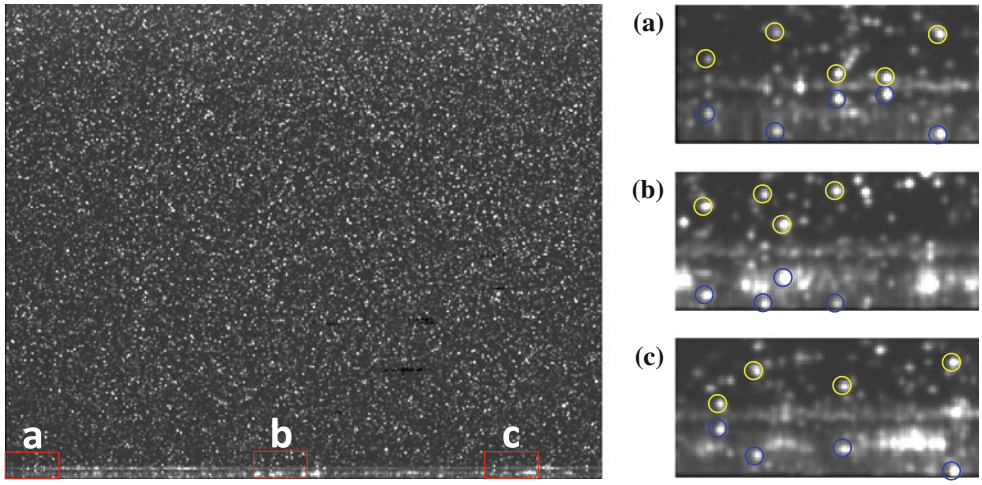

Fig. 4 Wall location detection: **a–c** close-up picture of the interface between flow and *solid wall* in a filtered PIV image. Tracer images are marked by *yellow circles*, while their mirror images are marked by *blue circles*

Secondly, image quality may be degraded due to the reflection from the boundary surface. In order to minimize the effects of wall reflection, the laser power was adjusted carefully. Furthermore, the glass of the test section was cleaned about every half an hour to remove any sedimentation particles. A Gaussian blur filter was also applied to process the raw pictures to reduce the background noise, as shown in Fig. 5a, c. The particle mask correlation method (Kazuo and Hang-Yu 2000) was used to identify the individual tracer image (Fig. 5b, d) and quantitatively examine the tracer particle density in the measurement region. As shown in Fig. 5e, the effective tracer particle density (N_{seed}) is quite uniform in the whole measurement region. Generally, in the near-wall region, there are about five tracer particle images in one interrogation window for the single-phase flow and four images for the two-phase flow, which is sufficient for performing a reliable cross-correlation in the present small interrogation window (Raffel et al. 2001).

Thirdly, the velocity gradient near the wall can increase the precision uncertainty of PIV measurement (Prasad et al. 1992, Raffel et al. 2001, Cameron 2011). In order to minimize this uncertainty, small interrogation window (32 × 16 pixels, with 50 % overlap in the x direction) was used in the present experiments (Raffel et al. 2001). Figure 6a shows the distribution of velocity gradient within interrogation windows, which is based on the time-averaged streamwise velocity of the DNS for the single-phase flow at $Re_\tau = 395$ (Kim et al. 1990), similar to the Re_τ (=430) in the present experiments. Correspondingly, the measurement uncertainty caused by the velocity gradient is plotted in Fig. 6b, which is determined based on the relation provided by Raffel et al. (2001). It is observed that the streamwise velocity gradient increases with the wall approached. The maximum gradient reaches 0.22 pixel/pixel at $y^+ \approx 2$ (0.07 mm), resulting in an uncertainty of 0.65 pixels, corresponding to 0.28 m × s^{-1}. For the two-phase flow, the presence of the particles increases the streamwise velocity of the gas-phase near the wall (which will be discussed in Sect. 3.2), hence reducing the velocity gradient relative to that of the single-phase flow. This means that the uncertainty due to velocity gradient is smaller for the two-phase flow.

Based on the discussions above, the precision limit of the time-averaged streamwise velocity of the single-phase flow for 95 % confidence interval (c.i.) is plotted in Fig. 7 (Stern et al. 1999). In the near-wall region, the maximum absolute uncertainty (normalized by u_τ) is estimated to be within ±0.63 at $y^+ \approx 2$. At $y^+ > 10$, the maximum absolute uncertainty is estimated to be less than ±0.29. Obviously, the measurement uncertainty reduces rapidly with increasing y^+. The relative experimental uncertainty of the time-averaged velocities is estimated to be within ±2.9 % in most measurement region ($y^+ > 10$), while within ±12.5 % in the near-wall region ($y^+ \approx 5.6$). Correspondingly, the uncertainty of the velocity fluctuations is estimated to be within ±6 % for $y^+ > 10$. Tables 3 and 4 list the PIV setting parameters and the corresponding uncertainties, respectively.

3 Results and discussions

3.1 Results of single-phase flow

To provide a benchmark, 2000 image pairs of the single-phase flow were captured. The time-averaged streamwise velocity (U^+), root-mean-square (r. m. s) value of fluctuation velocities (u^+_{rms} and v^+_{rms}) and Reynolds shear stress ($-\langle u'v'\rangle^+$) are presented in Fig. 8. The DNS results of Kim et al. (1990) at $Re_\tau = 395$ are also included for comparison.

As shown in Fig. 8a, the present PIV-measured U^+ almost overlaps with the DNS result, with the maximum

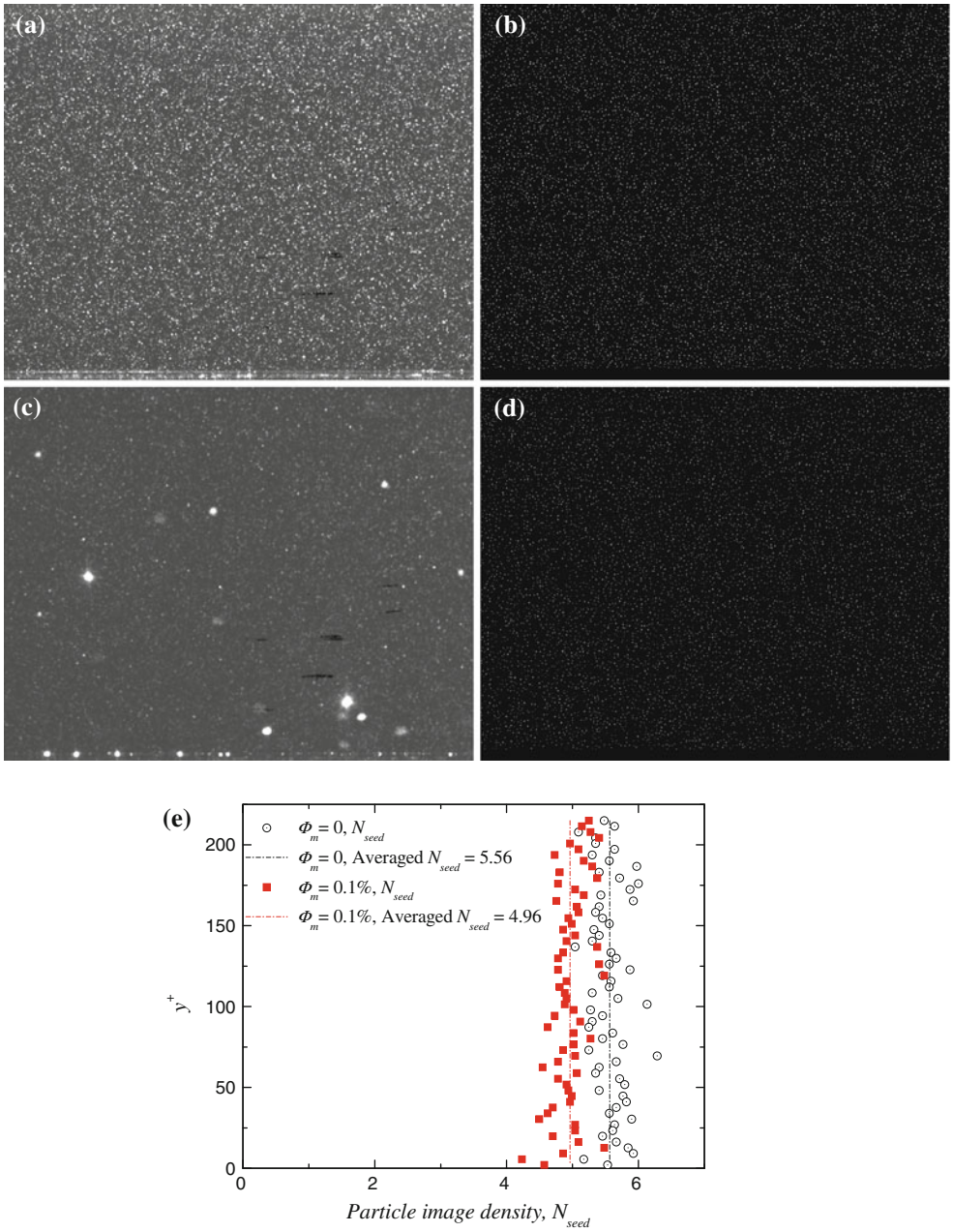

Fig. 5 Tracer identification and density: **a**, **c** filtered image, **b**, **d** identified tracer particles with mask correlation (cross-correlation threshold = 0.7); **a**, **b** $\Phi_m = 0$ (single-phase flow), **c**, **d** $\Phi_m = 0.1$ % (two-phase flow); **e** distribution of tracer image density, N_{seed}

difference of less than 1 % for $y^+ > 8$. The difference of u^+_{rms} is less than 5 % for $20 < y^+ < 180$, as shown in Fig. 8b. For v^+_{rms}, as shown in Fig. 8c, this difference is less than 13 % for $15 < y^+ < 40$ and within 6 % for $y^+ > 40$. The difference of $-\langle u'v'\rangle^+$ (Fig. 8d) is less than 5 % for $30 < y^+ < 150$. Generally, the maximum difference between the present PIV measurement results and those of the DNS at similar Re_τ (Kim et al. 1990) is less than 6 % for $y^+ > 40$ (apart from the wall), and between 8 and 15 % for $10 < y^+ < 40$ (near the wall).

3.2 Mean velocity and turbulent intensities of two-phase flow

Figure 9 presents the distribution of U^+, u^+_{rms}, v^+_{rms} and $-\langle u'v'\rangle^+$ for the gas-phase at $\Phi_m = 0$ (single-phase flow), 0.025, 0.1 and 0.5 %. The results of the particle-phase at $\Phi_m = 0.5$ % is also included for comparison. It is observed that, with the presence of the particles, U^+ of the gas-phase increases in the vicinity of the bottom wall ($y^+ \approx < 10$–17), while slightly decreasing in the outer region relative to

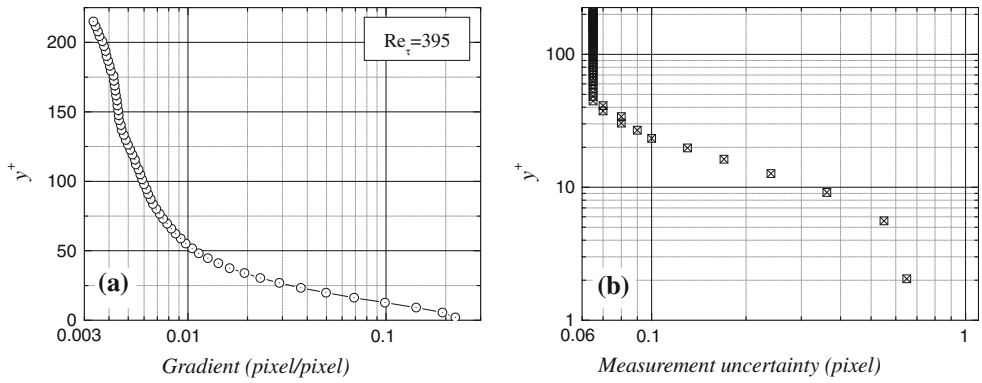

Fig. 6 Streamwise velocity gradient and the corresponding PIV uncertainty: **a** streamwise velocity gradient within interrogation windows, which is based on the time-averaged streamwise velocity of the DNS for the single-phase flow at $Re_\tau = 395$ (Kim et al. 1990); **b** PIV uncertainty due to velocity gradient, which is determined from reference graphs provided by Raffel et al. (2001)

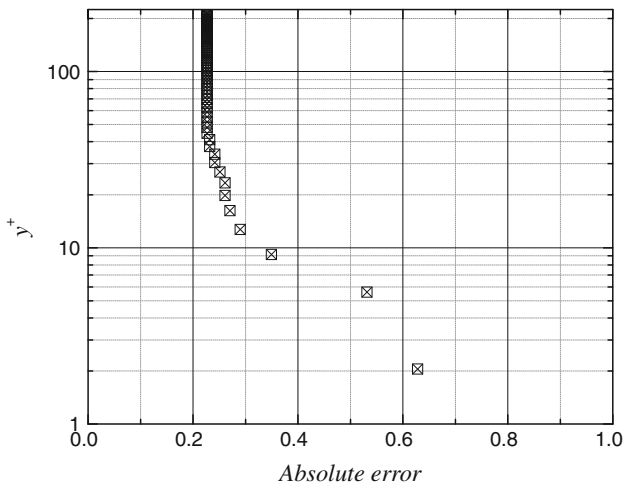

Fig. 7 The absolute uncertainty (normalized by u_τ) of the time-averaged streamwise velocity of the single-phase flow at 95 % confidence interval

Table 4 Main sources of PIV measurement uncertainties

PIV parameter	Typical value	Uncertainty (pixel)[a]
Background noise	5 %	<0.03
Image quantization levels (bit × pixel^{-1})	8	<0.03
Tracer particles per interrogation window	5.0–6.3 (particle-free)	<0.05
	4.2–5.5 (particle-laden)	<0.06
Tracer particle image diameter (pixel)	2.5	<0.06
Velocity gradient (max.) (pixel/pixel)	0.22	<0.65

[a] The uncertainty estimates are determined based on the relation provided by Raffel et al. (2001), which were originally obtained from PIV simulation studies for various conditions. A displacement of 1 pixel is equivalent to 0.43 m × s^{-1} in the present experiments

Table 3 PIV experiment setting parameters

PIV parameter	Typical value
Laser power (mJ)	120
Frame interval (μs)	18
Focal length of lens (mm)	105
Aperture (f number)	f2.8
PIV spatial resolution (μm × pixel^{-1})	7.785
Light sheet thickness (mm)	0.5
Diameter of tracer (μm)	5
Sampling rate (pairs × s^{-1})	3.75
Interrogation window size (pixels)	32 × 16 (50 % overlap in the x direction)

that of the single-phase flow, as shown in Fig. 9a. With the increase in Φ_m, this observation becomes more obvious, while the position that differentiates between increase and decrease also slightly shifts to the bottom wall. Considering the no-slip boundary condition, the increasing of U^+ near the wall indicates a decreasing thickness of the viscous sublayer and an increasing streamwise velocity gradient in the viscous sublayer.

Examining the U^+ of the particle-phase (Fig. 9a), it is obvious that the particle consistently lags behind the fluid, except very close to the wall. Such velocity distributions are similar to those observed by previous researchers for both gas–solid (Tsuji and Morikawa 1982; Tanière et al. 1997) and liquid–solid (Kaftori et al. 1995; Kiger and Pan 2002) flows. Very close to the wall, U^+ of the gas-phase reduces sharply under the effect of viscosity. Meanwhile, the reduction in U^+ for the particle-phase is slow as the bottom wall approached, because the inertia of the particle-phase is far larger than that of the gas-phase.

In addition to U^+, the presence of the particles also significantly modifies the turbulence intensities. Figure 9b depicts the distribution of u^+_{rms}. It can be found that the maximum of u^+_{rms} occurs at $y^+ = 10$–20 for the single-phase flow. However, under the effect of particles, the u^+_{rms} of the gas-phase gradually increases with the bottom wall approaching in the whole measurement region. The peak of u^+_{rms} in the single-phase flow enhances and shifts to the

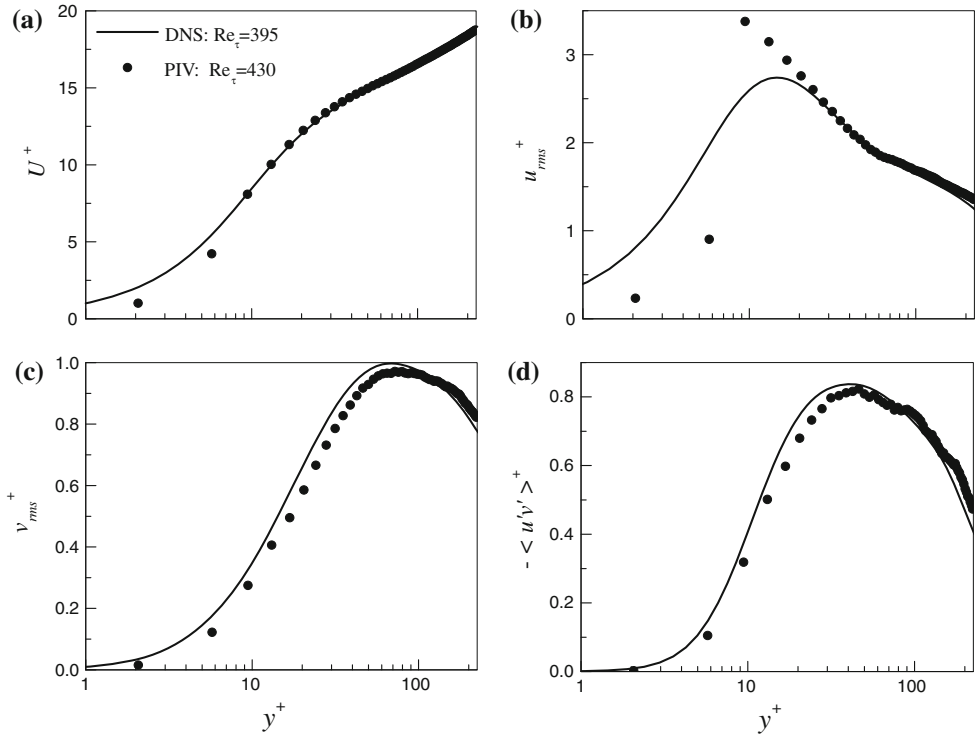

Fig. 8 PIV and DNS results (Kim et al. 1990) for single-phase flow: **a** time-averaged streamwise velocity, U^+, **b** r.m.s of streamwise fluctuation velocity, $u^+_{\rm rms}$, **c** r.m.s of wall-normal fluctuation velocity, $v^+_{\rm rms}$, and **d** Reynolds shear stress, $-\langle u'v'\rangle^+$

bottom wall with the presence of the particles for all tested Φ_m. At $y^+ > 30$, the $u^+_{\rm rms}$ of the gas-phase is enhanced with increasing Φ_m, while it is suppressed at $10 < y^+ < 30$. This phenomenon is similar to those reported by Tanière et al. (1997), Kiger and Pan (2002), Righetti and Romano (2004). It is worth mentioning that very close to the wall ($y^+ < 10$), the $u^+_{\rm rms}$ of the gas-phase is significantly larger than that of the single-phase flow. The roughness elements can significantly decrease the peak value of $u^+_{\rm rms}$ (Grass 1971, Bhaganagar et al. 2004, Jiménez 2004), which is different from that observed in the present experiment, as shown in Fig. 9b. Consequently, the enhancement of $u^+_{\rm rms}$ at $y^+ < 10$ may be mainly ascribed to the increased velocity gradient in the viscous sublayer (Fig. 9a), rather than the rough-wall effect due to particle sedimentation on the bottom wall (Kiger and Pan 2002; Chan-Braun et al. 2010).

With the presence of the particles, the $v^+_{\rm rms}$ of the gas-phase is remarkably enhanced at $y^+ \approx < 20$, while being slightly suppressed at $y^+ \approx > 20$, especially for a larger Φ_m, as shown in Fig. 9c. Similar behaviour of $v^+_{\rm rms}$ was also observed by Kiger and Pan (2002), Righetti and Romano (2004) and Chan-Braun et al. (2010). Since the roughness can noticeably enhance the cross-shear transport process along the wall-normal direction, especially for the inner region of a boundary layer ($y^+ < 10$) (Grass 1971; Bhaganagar et al. 2004; Jiménez 2004), the increase in $v^+_{\rm rms}$ near the wall in the present two-phase flow is generally considered to be caused by the rough-wall effect (Kiger and Pan 2002; Chan-Braun et al. 2010). In addition, the attenuation of $v^+_{\rm rms}$ in the buffer and logarithmic region is related to the suppressions of coherent structures by the presence of the particles, which will be discussed in detail later.

The effect of particles on the $-\langle u'v'\rangle^+$ of the gas-phase, as shown in Fig. 9d, is qualitatively similar to their effect on $v^+_{\rm rms}$. For example, at $y^+ \approx < 10$, the presence of the particles enhances the $-\langle u'v'\rangle^+$ of the gas-phase relative to that of the single-phase flow, whereas at $y^+ \approx > 10$, the $-\langle u'v'\rangle^+$ of the gas-phase is suppressed. Similar observation was also reported by Righetti and Romano (2004) at a much higher Φ_m.

As shown in Fig. 9b, the $u^+_{\rm rms}$ of the particle-phase is noticeably larger than that of the gas-phase in the whole measurement region. Similar observation was also reported by Tsuji and Morikawa (1982), Tanière et al. (1997) and Wu et al. (2006). In contrast, the $v^+_{\rm rms}$ of the particle-phase is larger than that of the gas-phase in the buffer region ($10 < y^+ < 30$), while being smaller in the outer region ($y^+ > 30$), as shown in Fig. 9c. In addition, Fig. 9d also shows the $-\langle u'v'\rangle^+$ of the particle-phase is smaller than that of the gas-phase at $y^+ \approx < 40$, while being larger than the later at $y^+ \approx >40$. Obviously, there is a significant difference between particle- and gas-phase turbulence statistics. This may be ascribed to the particle velocity fluctuations, which are not only related to the gas turbulence, but also to the inertia and gravity effects (Tanière et al. 1997).

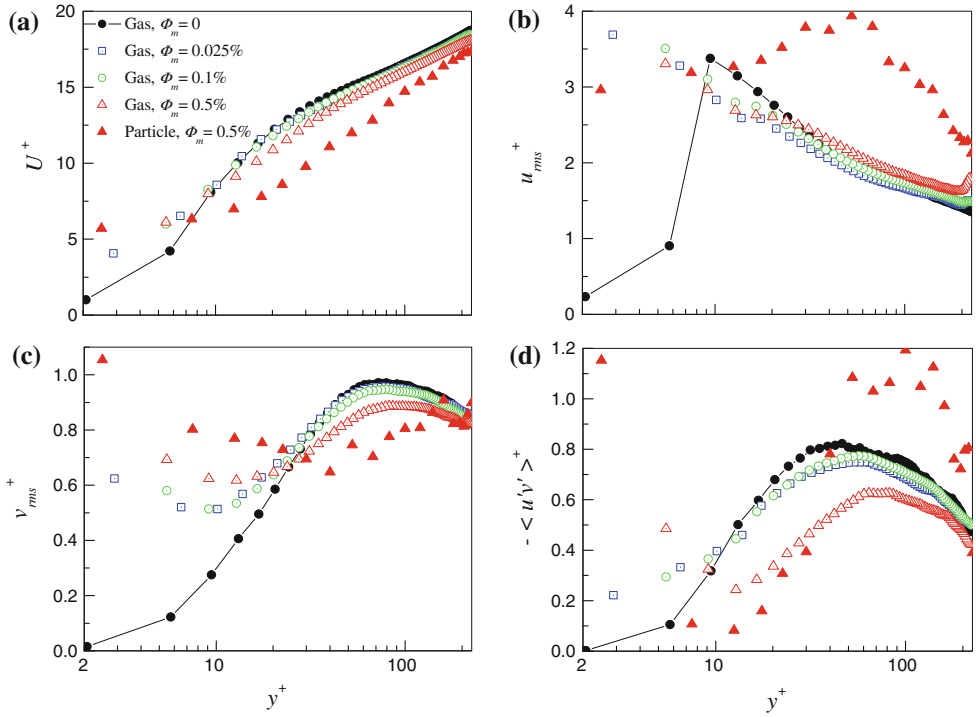

Fig. 9 Distribution of U^+, $u^+_{\rm rms}$, $v^+_{\rm rms}$ and $-\langle u'v'\rangle^+$ of gas-phase at $\Phi_m = 0$ (single-phase flow), 0.025, 0.1 and 0.5 %, and of particle-phase at $\Phi_m = 0.5$ %, **a** U^+, **b** $u^+_{\rm rms}$, **c** $v^+_{\rm rms}$, **d** $-\langle u'v'\rangle^+$

3.3 Particle behaviour

The characteristic of particle behaviour is a key factor that determines the mechanism of turbulence modification. To understand the particle behaviour better, it is interesting to investigate the conditionally sampled U^+, $u^+_{\rm rms}$ and $v^+_{\rm rms}$ for the particle-phase based on its instantaneous velocity in the wall-normal direction (upward or downward), as shown in Fig. 10. Obviously, the U^+ of the downwards moving particles is larger than that of the upwards moving particles (Fig. 10a). This is because most upwards moving particles are rebound from the bottom wall (Tanière et al. 1997) and they have a smaller U^+ due to the kinetic energy loss in the particle–wall collisions. However, for the downwards moving particles, they have been carried by and obtain kinetic energy from the fluid before wall collisions, thus resulting in a larger U^+. The present results validate the argument proposed by Tanière et al. (1997), who investigated the particle behaviour near the bottom wall of a horizontal channel and suggested that the U^+ of the upwards-moving particles should be smaller than that of the downwards-moving ones.

As shown in Fig. 10b, the $u^+_{\rm rms}$ of the upwards-moving particles is larger than that of the downwards-moving particles at $y^+ \approx >30$. This observation may also be ascribed to the effect of particle–wall collision. Since the trajectories and impact angles of particles are different from each other, their kinetic energy loss may also be different (Sommerfeld and Huber 1999), which results in a large variation of streamwise velocity, that is, a large value of $u^+_{\rm rms}$. Contrarily, after a period of acceleration, the $u^+_{\rm rms}$ of the downwards-moving particles is closer to that of the gas-phase and smaller than that of the upwards-moving particles.

For a rigid smooth wall, the restitution coefficient (e) of normal velocity component in particle–wall collision is close to 1 and nearly independent of the impact angle (Sommerfeld and Huber 1999).That is, the effect of particle–wall collision on $v^+_{\rm rms}$ is relatively small. Consequently, the values of $v^+_{\rm rms}$ for the upwards- and downwards-moving particles are similar to each other and about one half of the unconditionally averaged value, as shown in Fig. 10c.

Since turbulence is a multi-scale system, particles are only at the mercy of the wall-generated turbulence whose time scale is much larger than that of the particles (Eaton and Fessler 1994; Kulick et al. 1994). For the liquid–solid flow, the particle relaxation time is generally much smaller than or approximately equal to the smallest (Kolmogorov) time scale of the turbulence. So the particle behaviour is governed by the turbulence coherent structures and characterized by a pure suspension (Rashidi et al. 1990; Kaftori et al. 1998; Kiger and Pan 2002; Righetti and Romano 2004; Hout 2011). Contrarily, for the present gas–solid flow, the particle relaxation time is much larger than the Kolmogorov time scale of the turbulence, as shown in Table 2. So the gas-phase turbulent fluctuation cannot obviously influence the particle motion. And the particle velocity fluctuations are mainly governed by inertia and gravity effect.

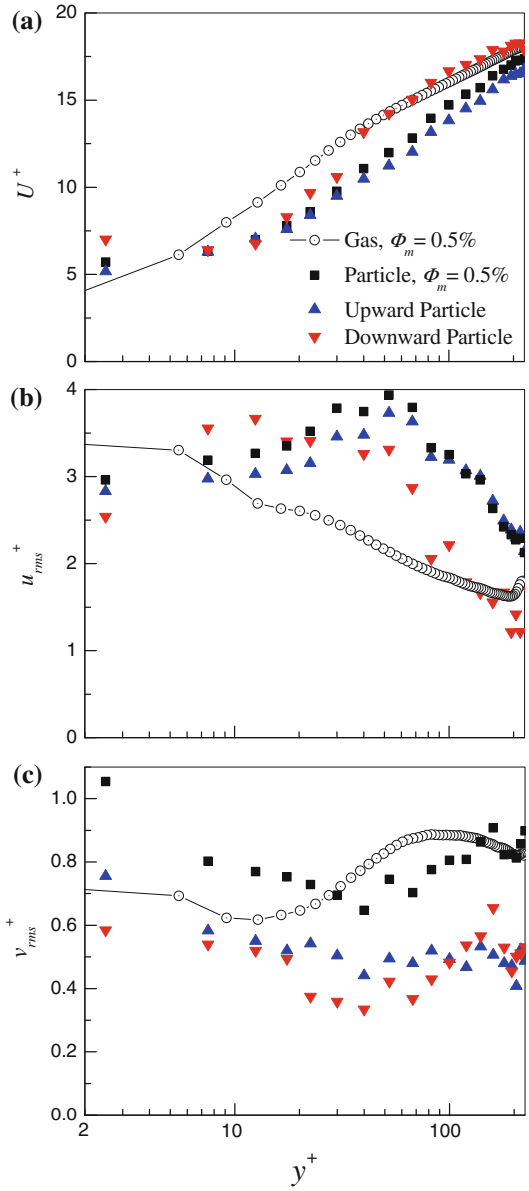

Fig. 10 Turbulence statistics for upwards-and downwards-moving particles: **a** U^+, **b** u^+_{rms}, **c** v^+_{rms}

The particle volume fraction (Φ_v) and mass loading ratio (Φ_m) can be estimated based on the number of particles presented in certain bin (as shown in Fig. 3) and the thickness of laser sheet. The distribution of Φ_v and Φ_m is presented in Fig. 11 for the case of $\Phi_m = 0.5$ %. The corresponding distributions for $\Phi_m = 0.025$ and 0.1 % are qualitatively similar to those shown in Fig. 11, thus not presented here. The Φ_v increases with the bottom wall approached, and its maximum value appears at $y^+ \approx 10$ (0.35 mm). The maximum Φ_v is about 1×10^{-4} (as shown in Fig. 11), which is significantly smaller than the critical value of Φ_v for four-way coupling (Elghobashi 1994). This observation suggests that the interaction between particles and gas in the present experiments is two-way coupling in the whole measurement region.

3.4 Modification of turbulent coherent structures

In addition to changing the macroscopic statistics of turbulence, the presence of the particles also affects the turbulent coherent structures. The spatial two-point correlation coefficients, R_{uu} and R_{vv}, can be used as a measure for the scale of coherent structures (Moin and Kim 1985; Bhaganagar et al. 2004), which are defined as Eq. (4):

$$R_{u_iu_i}(x,y) = \frac{\overline{u_i'(x_{\mathrm{ref}},y_{\mathrm{ref}}) \times u_i'(x,y)}}{\sqrt{\overline{u_i'(x_{\mathrm{ref}},y_{\mathrm{ref}})^2}} \times \sqrt{\overline{u_i'(x,y)^2}}} \tag{4}$$

where the over-bar denotes that the time-average, (x_{ref}, y_{ref}) indicates the reference point.

Figure 12 shows the distribution of R_{uu} and R_{vv} for $\Phi_m = 0$ and 0.5 %. The reference point is at $x = 4.98$ mm and $y = 1.25$ mm ($y^+ = 30$). The distributions of R_{uu} and R_{vv} for $\Phi_m = 0.025$ and 0.1 % are qualitatively similar to that for $\Phi_m = 0.5$ %, thus not present here. The distributions of R_{uu} and R_{vv} are connected to the properties of turbulence coherent structures. For the present tested turbulent boundary layer, R_{uu} and R_{vv} indicate the information about streamwise structure extent and spanwise vortex diameter, respectively (Moin and Kim 1985; Bhaganagar et al. 2004). Both R_{uu} and R_{vv} contours shrink considerably under the effects of particles (as shown in Fig. 12), which suggests the reduction in both streamwise structure and spanwise vortex scale.

However, based on the DNS results for a downward vertical channel flow, Dritselis and Vlachos (2008) found the addition of the particles elongate the quasi-streamwise vortices although their strength weakened. In other words, the flow direction, for example, horizontal or vertical, plays an important role in the effect of particles on the coherent structures in channel flow. In the present horizontal channel, the characteristic of particle behaviour, including the intensified saltation (as shown in Fig. 10) and sedimentation (as shown in Fig. 11) near the bottom wall, indicates that both crossing-trajectory effects and rough-wall effects are enhanced, which reduces the scale of the quasi-streamwise turbulent structures.

In addition, for the single-phase channel flow, the inclination angle of the principal axis of R_{uu} contours is about 9° (as shown in Fig. 12a), similar to the inclination angle of the mean quasi-streamwise vortex observed by Dritselis and Vlachos (2008). Despite the R_{uu} contours shrink considerably with the presence of the particles, there is no obvious change in this inclination angle, as shown in Fig. 12c.

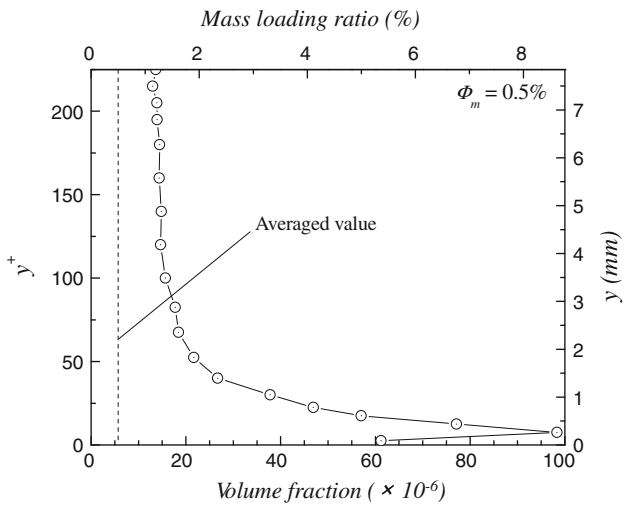

Fig. 11 Distribution of particle volume fraction and mass loading ratio for $\Phi_m = 5 \times 10^{-3}$

Although there are some particles settling on the bottom wall (as shown in Fig. 5c), the density of the sedimentation particles on the wall is very small. Besides that, the diameter of the sedimentation particles is only about 1.71 in wall units. The equivalent roughness due to these sedimentation particles would not cause a significant modification of the turbulence coherent structures in the buffer region, as shown in Fig. 12 (Grass 1971; Bhaganagar et al. 2004; Jiménez 2004). Therefore, it may be deduced that, besides the rough-wall effect due to the particles sedimentation on the bottom wall, the crossing-trajectory effect is also an important factor to reduce the spatial scale of the coherent structures near the wall (especially for the buffer region).

Figure 13 presents two typical instantaneous vector maps of the gas velocity fluctuations (Reynolds decomposed) to illustrate the decrease in the spanwise vortex size under the effects of particles. Following Kline and Robinson (1989), a vortex is defined as the region of concentrated vorticity around which the pattern of streamlines is roughly circular when viewed in a frame moving with the centre of the vortex. The vortex identification method used presently is similar to that proposed by Adrian et al. (2000), meanwhile a modified swirling-strength parameter proposed by Wu and Christensen (2006) is also used to detect the vortex cores, which is defined as:

$$\Lambda_{ci}^{+}(x,y) = \frac{\Lambda_{ci}(x,y)}{u_\tau^4/\nu^2} = \frac{\lambda_{ci}(x,y)}{u_\tau^4/\nu^2} \times \frac{\omega_z(x,y)}{|\omega_z(x,y)|} \quad (5)$$

where $\lambda_{ci}(x, y)$ is the local velocity-gradient tensor, and ω_z is the spanwise vorticity.

As shown in Fig. 13, the addition of the particles reduces the spanwise vortex size and the interspacing between vortices, relative to those of the single-phase flow. This result coincides with the modulation of R_{uu} and R_{vv}, as shown in Fig. 12. Pay special attention to the vortices A, B and C in Fig. 13b, counter-rotating vortices appear on both sides of the particle settlement path. Based on the characteristic of particle behaviour in the gas-particle flow, this phenomenon depicts the picture that a group of particles are breaking up a large-scale turbulence structure near the wall. For each tested case, about 600 instantaneous flow fields were visually checked. For the single-phase flow ($\Phi_m = 0$), there are about 80 % instantaneous flow fields qualitatively similar to that shown in Fig. 13a, containing several larger-scale vortices. However, for $\Phi_m = 0.5$ %, about 50 % instantaneous flow fields capture the break-up process of vortex, similar to that shown in Fig. 13b.

Quadrant analysis of the Reynolds shear stress can provide detailed information on the contribution to the total turbulence production from various events occurring in the flows (Willmarth and Lu 1972, Kim et al. 1987). Following Kim et al. (1987), four-quadrant events are defined in the present paper: Q1 event with $u' > 0$ and $v' > 0$; Q2 event (ejection) with $u' < 0$, $v' > 0$; Q3 event with $u' < 0$, $v' < 0$; and Q4 event (sweep) with $u' > 0$, $v' < 0$. Obviously, Q2 and Q4 events contribute to the positive productions of both Reynolds shear stress and TKE, while Q1 and Q3 events contribute to the negative productions of them.

Figure 14 shows the fractional contribution to the total Reynolds shear stress from each quadrant for $\Phi_m = 0$, and the corresponding DNS results at a similar Re_τ (Kim et al. 1987) are also included for comparison. The present PIV measurement result corresponds well with that of the DNS, which provides a validation for the present measurement and analysis. As shown in Fig. 14, the contributions from Q1 and Q3 to the Reynolds shear stress are similar and almost unchanged in the whole measurement region, which is far smaller than those of Q2 and Q4. At $y^+ \approx <15$, the Reynolds shear stress is dominated by Q4 events (sweeps), while at $y^+ \approx >15$, Q2 events (ejections) dominate.

To get better understanding of the turbulence modulation caused by particles, condition-average for the $-\langle u'v'\rangle^+$ of the gas-phase is conducted for the four-quadrant events for the single-phase flow ($\Phi_m = 0$) and the three tested Φ_m, as shown in Fig. 15. The Reynolds shear stress from Q2 and Q4 events, which corresponds to the positive production of TKE, increases at $y^+ \approx <15$ and decreases at $y^+ \approx >15$ with increased Φ_m, as shown in Fig. 15b, d. This observation suggests that both 'ejection' and 'sweep' events are enhanced by the presence of the particles near the wall ($y^+ \approx <15$), while being suppressed in the outer region ($y^+ \approx >15$). Considering the fact that ejection events (Q2) dominate at $y^+ \approx >15$ (see Fig. 14), the reduction in Reynolds shear stress in the outer region (as

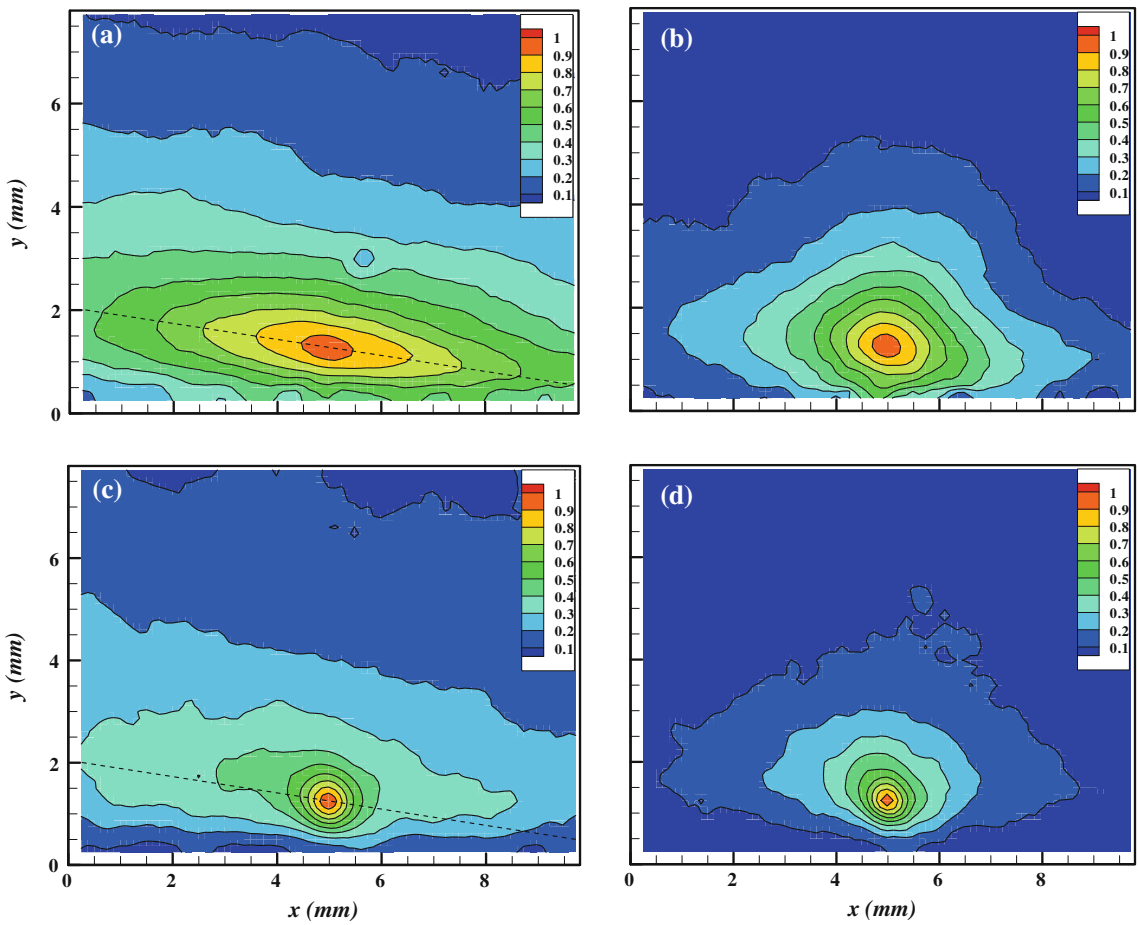

Fig. 12 Two-point correlation coefficients of gas-phase; the lateral position of the reference point is $y^+ = 30$: **a**, **c** R_{uu}, **b**, **d** R_{vv}; **a**, **b** $\Phi_m = 0$ (single-phase flow), **c**, **d** $\Phi_m = 0.5$ %

shown in Fig. 9d) may be mainly ascribed to the suppression of Q2 events rather than Q4 events. On the other hand, the Reynolds shear stresses from Q1 and Q3 events, which are the negative contribution for TKE, are remarkably increased in all measurement range.

Similar observation was found by Righetti and Romano (2004) in a horizontal liquid-particle channel flow. They attributed the weakening of turbulence bursting (Q2 events) to the momentum transfer in the process of particle lift-up by the fluid ejections. However, in the present gas-particle channel flow, the particle relaxation time is larger than the time scale of the large turbulence structures in the whole measurement region (as listed in Table 2). This suggests that the particle transverse motion is dominated by the particle–wall collision under the effect of inertia and gravity rather than the fluid entrainment, that is, ejections and sweeps. Presumably, in the present gas-particle flow, the suppression of Q2 and Q4 events in the buffer and logarithmic region (Fig. 15b, d) should be attributed to the breaking of coherent structures caused by the crossing-trajectory effect of particles. On the other hand, the augment of Q2 and Q4 events near the bottom wall is related to the intensified cross-shear transport process along the wall-normal direction caused by the effect of rough-wall.

The presence of the particles changes not only the strength of turbulence bursting near the wall, but also its frequency (Kaftori et al. 1998). The frequency of wall structures can be evaluated by examining the probability of the four quadrant events, as shown in Fig. 16. This probability is defined as:

$$\text{Probability}\left(i_q, y^+\right) = \frac{\sum_{\text{sample}} \left(\text{Number}(i_q, y^+)\right)}{\sum_{\text{sample}} \left(\sum_{i=1}^{4} \text{Number}(i_q, y^+)\right)}, \quad i_q = (1, 2, 3, 4) \tag{6}$$

where *sample* is the number of the instantaneous velocity fields captured for one case.

Generally, the presence of the particles reduces the probability of Q4 events, while increasing that of Q1, Q2 and Q3 events. The effect of particles on the four-quadrant events is remarkable at $y^+ < 80$ (especially for $10 < y^+ < 30$), while becoming less obvious at $y^+ > 80$, as shown in Fig. 16. Presumably, this observation may be related to

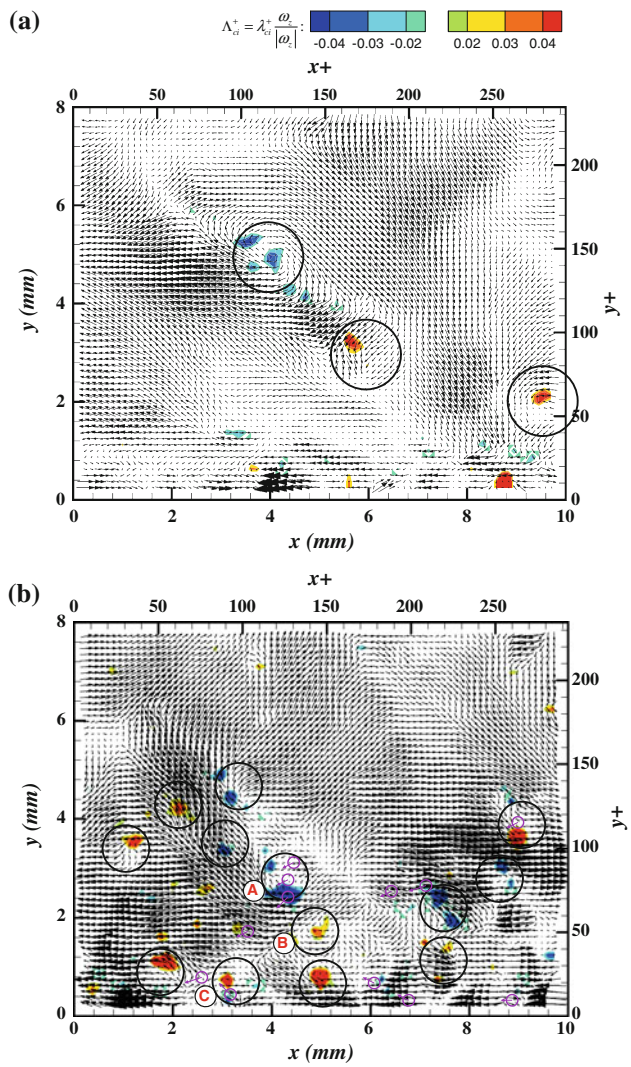

Fig. 13 Typical instantaneous flow fields of gas velocity fluctuations (Reynolds decomposed): **a** $\Phi_m = 0$, **b** $\Phi_m = 0.5$ %. Gas vectors are *black*, while particle location and velocity vectors are *purple*. A modified swirling-strength parameter (Λ_{ci}^{+}) proposed by Wu and Christensen (2006) is indicated by the *colour blocks map*. Vortex structures are marked by *black circles*

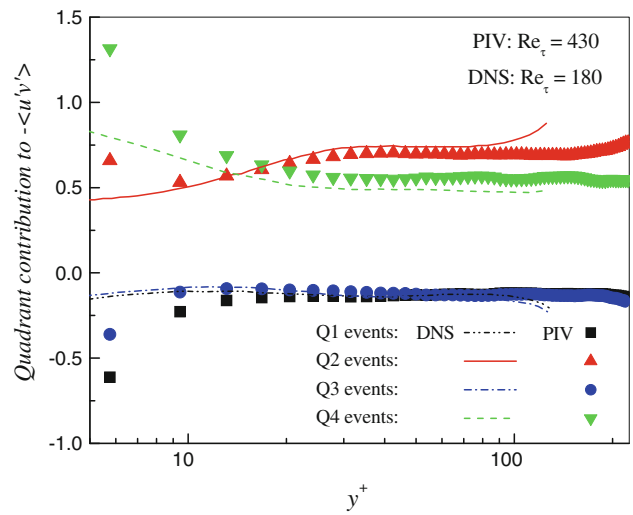

Fig. 14 Reynolds shear stress from each quadrant normalized by local time-averaged Reynolds shear stress: comparison of single-phase PIV results with DNS results of Kim et al. (1987)

the fact that the coherent structures prevail in the buffer and lower logarithmic region (Jeong et al. 1997; Robinson 1991).

With the presence of the particles, the reduction in Q4 events is more remarkable than the increase in Q2 events (Fig. 16b, d), similar to that observed by Pan and Banerjee (1996). For example, at $y^+ = 30$, the probability of Q2 events increases from 27 % for the single-phase flow to 29 % for $\Phi_m = 0.5$ %, while the corresponding probability of Q4 events reduces from 40 to 32 %. That is, the total probability of both Q2 and Q4 events (ejections and sweeps) are reduced by the presence of the particles. In view of the fact that the Q2 and Q4 events are related to the coherent structures in the boundary layer (Jeong et al. 1997), the decrease in their total probability suggests that the occurrence of coherent structures is suppressed.

Figure 17 presents the particle distribution in the four quadrants for the case of $\Phi_m = 0.5$ % at three typical y^+. Note that, the particle fluctuation velocities in the present paper, for example, u_p' and v_p', are relative to the local time-averaged gas-phase velocity, which can highlight the effect of particles on the gas-phase flow. Here, the terminologies of quadrant analysis are used to simplify the following discussions.

At $y^+ = 10$ (viscous sublayer), most particles reside in the second quadrant (Q2), with the probability of 58.6 % (Fig. 17a), while, only 6.7 % of particles locate within the fourth quadrant (Q4). As y^+ reaches 30 (buffer region), the distribution of particles (Fig. 17b) is qualitatively similar to that at $y^+ = 10$. This is because, in the near-wall region, most particles rebound from the bottom wall and move upward ($v_p' > 0$), which have a smaller streamwise velocity relative to the local gas-phase velocity, due to the kinetic energy loss in wall collisions. At $y^+ = 150$ (outer region), 39.3 % of particles remain in the second quadrant (Q2), as shown in Fig. 17c, which indicates that the effect of wall collision on the particle behaviour decreases obviously in the outer region. It is worth mentioning that the probability of particles in the fourth quadrant (Q4) is always smaller than that in the second quadrant (Q2), especially at a smaller y^+.

To present the influence of the particles on the gas-phase more intuitively, Fig. 18 shows the probabilities of the four-quadrant events for both particles at $\Phi_m = 0.5$ % and gas-phase at $\Phi_m = 0$ and at three y^+. For the single-phase flow ($\Phi_m = 0$), the probability of the four-quadrant events is similar at y^+=10, 30 and 150. For example, probability of

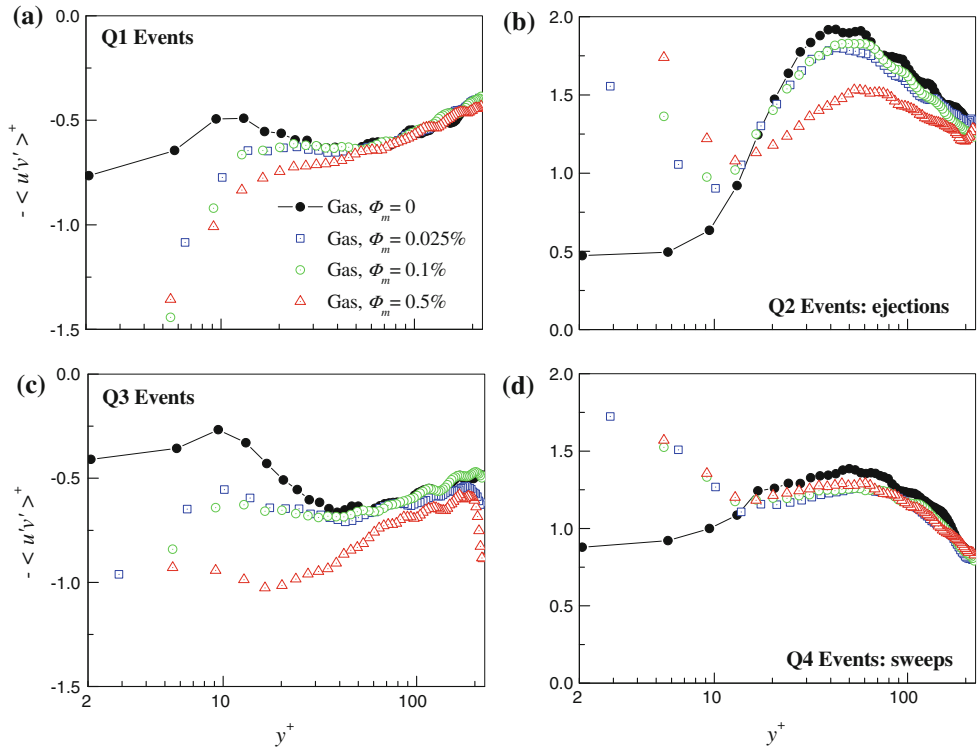

Fig. 15 Gas-phase Reynolds shear stresses from the four quadrant events at $\Phi_m = 0$, 0.025, 0.1 and 0.5 %

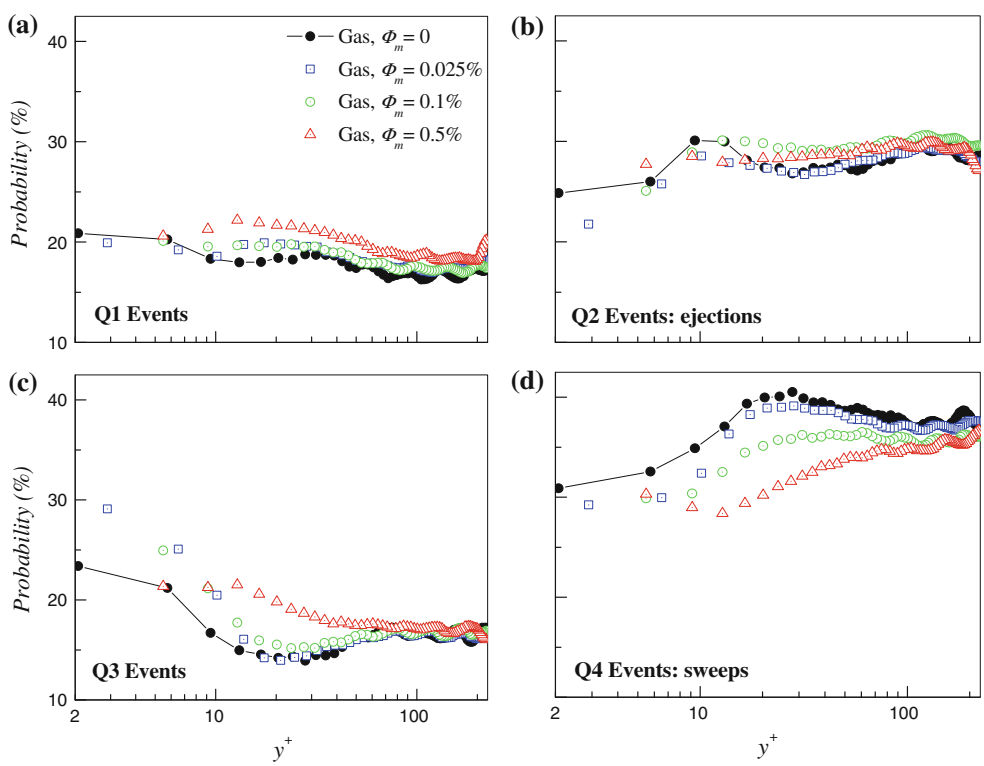

Fig. 16 Quadrant analysis of gas-phase: percentum of the four quadrant events

the Q4 events is always higher than that of the Q2 events and the Q2 and Q4 events predominate among all events, as shown in Fig. 18.

Contrarily, the probability of the four-quadrant events of particle-phase varies significantly with increasing y^+. At $y^+ = 10$ and 30, the probability of the Q2 events of the

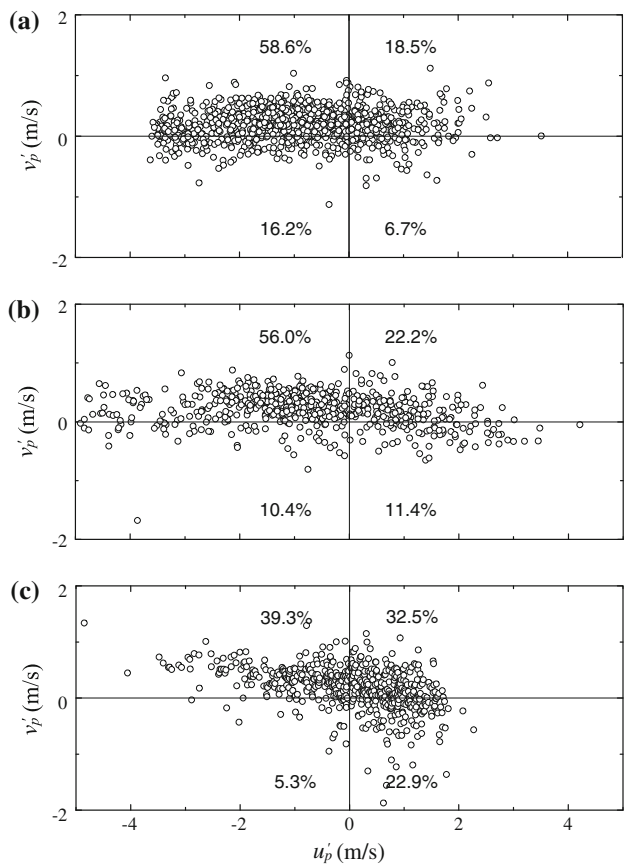

Fig. 17 Distribution of particle velocity fluctuations for $\Phi_m = 0.5$ % at three heights: **a** $y^+ = 10$, **b** $y^+ = 30$, **c** $y^+ = 150$

particles is far larger than that of the gas-phase, while the probability of the Q4 events of the former is significantly smaller than that of the later. This observation explains why the presence of the particles increases the Q2 events and suppresses the Q4 events of the gas-phase near the bottom wall, as shown in Fig. 16b, d. At $y^+ = 150$, the probabilities of the Q2 and Q4 events of the particles are close to those of the gas-phase (as shown in Fig. 18). Consequently, the effect of particles on the probability of the four-quadrant events of the gas-phase is less obvious at y^+=150 relative to that near the bottom wall, as shown in Fig. 16.

4 Conclusion

Turbulence modulation in the lower boundary layer of a dilute gas-particle horizontal channel flow was experimentally investigated using a simultaneous two-phase PIV technique. Three low mass loadings ratios (Φ_m) ranging from 10^{-4} to 10^{-3} are tested. From the experimental results, following conclusions can be drawn:

1. The presence of the particles ($\rho_p/\rho_f = 877$) can distinctly modify the gas-phase characteristics in macro-scale, for example, u^+_{rms}, v^+_{rms} and $-\langle u'v'\rangle^+$, through the effects on the turbulent coherent structures in meso-scale near the wall, even at $\Phi_m = 0.025$ %. This turbulence modulation becomes more obvious with increasing particle mass loading.
2. Due to the particle inertia, the presence of the particles increases the U^+ of the gas-phase near the wall ($y^+ \approx$ <10–17), while reducing it away from the wall. It changes the viscous sublayer of gas turbulence with a smaller thickness and a larger streamwise velocity gradient, which increases the peak value of the u^+_{rms} of the gas-phase with its location shifting to the wall.
3. In the present horizontal channel, particles tend to deposit on the bottom wall under the effect of gravity, which is equivalent to augment the roughness of the bottom wall. As a result of this, the v^+_{rms} and $-\langle u'v'\rangle^+$ of the gas-phase significantly increase in the inner region of the boundary layer ($y^+ < 10$). On the other hand, the addition of the particles ($d_p^+ = 1.71$) suppresses the gas turbulent coherent structures, which noticeably reduces the v^+_{rms} and $-\langle u'v'\rangle^+$ of the gas-phase in the outer region of the boundary layer ($y^+ > 20$).

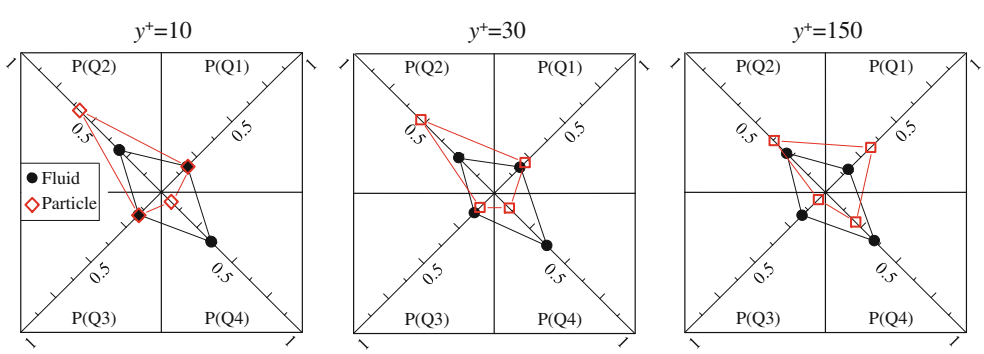

Fig. 18 Probability of the four-quadrant events of particle and fluid at different height for $\Phi_m = 0.5$ %

4. The spatial scale of the wall structures remarkably shrinks under the intensified crossing-trajectory effects due to particle saltation near the bottom wall.
5. Under the effect of particle–wall collision, the probability of particles in the fourth quadrant (Q4) is always smaller than that in the second quadrant (Q2), especially at a smaller y^+. Therefore, the presence of the particles slightly increases the Q2 events (ejections) and obviously decreases the Q4 events (sweeps) of the gas-phase. As a result of this, the particles reduce not only the strength of turbulence bursting, but also its frequency.

Acknowledgments This study is supported by the National Basic Research Program of China (Grant No. 2010CB227004) and the National Natural Science Foundation of China (Grant No. 50721005, 50976042, 51006043).

References

Adrian RJ, Christensen KT, Liu ZC (2000) Analysis and interpretation of instantaneous turbulent velocity fields. Exp Fluids 29:275–290

Bhaganagar K, Kim J, Coleman G (2004) Effect of roughness on wall-bounded turbulence. Flow Turbul Combust 72:463–492

Brodkey RS, Wallace JM, Eckelmann H (1974) Some properties of truncated turbulence signals in bounded shear flows. J Fluid Mech 63:209–224

Brooke JW, Kontomaris K, Hanratty TJ, McLaughlin JB (1992) Turbulent deposition and trapping of aerosols at a wall. Phys Fluids A 4:825–834

Cameron SM (2011) PIV algorithms for open-channel turbulence research: accuracy, resolution and limitations. J Hydro Environ Res 5:247–262

Cantwell BJ (1981) Organized motion in turbulent flow. Annu Rev Fluid Mech 13:457–515

Chan-Braun C, García-Villalba M, Uhlmann M (2010) Numerical simulation of fully resolved particles in rough-wall turbulent open channel flow. In: Proceedings of the 14th international conference on multiphase flow, Tampa, USA

Ciccone AD, Kawall JG, Keffer JF (1990) Flow visualization/digital image analysis of saltating particle motions. Exp Fluids 9:65–73

Dritselis CD, Vlachos NS (2008) Numerical study of educed coherent structures in the near-wall region of a particle-laden channel flow. Phys Fluids 20:055103–055112

Eaton JK (1994) Experiments and simulations on turbulence modification by dispersed particles. Appl Mech Rev 47:S44–S48

Eaton JK (1995) Turbulence modification by particle in shear flows. ASME FED-228 gas-particle flows, pp 273–278

Eaton JK, Fessler JR (1994) Preferential concentration of particles by turbulence. Int J Multiphase Flow 20:169–209

Eckelmann H (1974) The structure of the viscous sublayer and the adjacent wall region in a turbulent channel flow. J Fluid Mech 65:439–459

Elghobashi S (1994) On predicting particle-laden turbulent flows. Appl Sci Res 52:309–329

Elghobashi S, Truesdell GC (1993) On the two-way interaction between homogeneous turbulence and dispersed solid particles. I: turbulence modification. Phys Fluids A 5:1790–1801

Gore RA, Crowe CT (1989) Effect of particle size on modulating turbulent intensity. Int J Multiphase Flow 15:279–285

Grass AJ (1971) Structural features of turbulent flow over smooth and rough boundaries. J Fluid Mech 50:233–255

Hagiwara Y, Murata T, Tanaka M, Fukawa T (2002) Turbulence modification by the clusters of settling particles in turbulent water flow in a horizontal duct. Powder Technol 125:158–167

Hetsroni G (1989) Particles-turbulence interaction. Int J Multiphase Flow 15:735–746

Hout Rv (2011) Time-resolved PIV measurements of the interaction of polystyrene beads with near-wall-coherent structures in a turbulent channel flow. Int J Multiphase Flow 37:346–357

Hussain AKMF (1986) Coherent structures and turbulence. J Fluid Mech 173:303–356

Jeong J, Hussain F, Schoppa W, Kim J (1997) Coherent structures near the wall in a turbulent channel flow. J Fluid Mech 332:185–214

Jiménez J (2004) Turbulent flows over rough walls. Annu Rev Fluid Mech 36:173–196

Kaftori D, Hetsroni G, Banerjee S (1995) Particle behavior in the turbulent boundary layer. II. Velocity and distribution profiles. Phys Fluids 7:1107–1121

Kaftori D, Hetsroni G, Banerjee S (1998) The effect of particles on wall turbulence. Int J Multiphase Flow 24:359–386

Kazuo O, Hang-Yu L (2000) Particle-tracking velocimetry with new algorithms. Meas Sci Technol 11:603

Khalitov DA, Longmire EK (2002) Simultaneous two-phase PIV by two-parameter phase discrimination. Exp Fluids 32:252–268

Kiger KT, Pan C (2002) Suspension and turbulence modification effects of solid particulates on a horizontal turbulent channel flow. J Turbul 3:N19

Kim HT, Kline SJ, Reynolds WC (1971) The production of turbulence near a smooth wall in a turbulent boundary layer. J Fluid Mech 50:133–160

Kim J, Moin P, Moser R (1987) Turbulence statistics in fully developed channel flow at low Reynolds number. J Fluid Mech 177:133–166

Kim J, Moin P, Moser R (1990) In: Bradshaw P (ed) The diskette of collaborative testing of turbulence models. Stanford University, Stanford

Kline SJ, Robinson SK (1989) Quasi-coherent structures in the turbulent boundary layer. Part I: status report on a community-wide summary of the data. In: Kline SJ, Afgan NH (ed) Near wall turbulence proceedings of zaric memorial conference, pp 218–247

Kline SJ, Reynolds WC, Schraub FA, Runstadler PW (1967) The structure of turbulent boundary layers. J Fluid Mech 30:741–773

Kulick JD, Fessler JR, Eaton JK (1994) Particle response and turbulence modification in fully developed channel flow. J Fluid Mech 277:109–134

Kussin J, Sommerfeld M (2002) Experimental studies on particle behaviour and turbulence modification in horizontal channel flow with different wall roughness. Exp Fluids 33:143–159

Li F, Qi H, You C (2010a) Phase Doppler anemometry measurements and analysis of turbulence modulation in dilute gas–solid two-phase shear flows. J Fluid Mech 663:434–455

Li J, Liu Z-H, Wang H-F, Chen S, Liu Y-M, Han H-F, Zheng C-G (2010b) Turbulence modulations in the boundary layer of a horizontal particle-laden channel flow. Chinese Phys Lett 27:064701

Liljegren LM, Vlachos NS (1990) Laser velocimetry measurements in a horizontal gas-solid pipe flow. Exp Fluids 9:205–212

Liu ZC, Landreth CC, Adrian RJ, Hanratty TJ (1991) High resolution measurement of turbulent structure in a channel with particle image velocimetry. Exp Fluids 10:301–312

Lu SS, Willmarth WW (1973) Measurements of the structure of the Reynolds stress in a turbulent boundary layer. J Fluid Mech 60:481–511

Marchioli C, Soldati A (2002) Mechanisms for particle transfer and segregation in a turbulent boundary layer. J Fluid Mech 468: 283–3158

Moin P, Kim J (1985) The structure of the vorticity field in turbulent channel flow. Part 1. Analysis of instantaneous fields and statistical correlations. J Fluid Mech 155:441–464

Owen PR (1969) Pneumatic transport. J Fluid Mech 39:407–432

Pan Y, Banerjee S (1996) Numerical simulation of particle interactions with wall turbulence. Phys Fluids 8:2733–2755

Parthasarathy RN, Faeth GM (1990) Turbulence modulation in homogeneous dilute particle-laden flows. J Fluid Mech 220: 485–514

Pedinotti S, Mariotti G, Banerjee S (1992) Direct numerical simulation of particle behaviour in the wall region of turbulent flows in horizontal channels. Int J Multiphase Flow 18:927–941

Prasad A, Adrian R, Landreth C, Offutt P (1992) Effect of resolution on the speed and accuracy of particle image velocimetry interrogation. Exp Fluids 13:105–116

Raffel M, Willert C, Werely S, Kompenhans J (2001) Particle image velocimetry: a practical guide. Springer, Berlin

Rashidi M, Hetsroni G, Banerjee S (1990) Particle-turbulence interaction in a boundary layer. Int J Multiphase Flow 16:935–949

Righetti M, Romano GP (2004) Particle–fluid interactions in a plane near-wall turbulent flow. J Fluid Mech 505:93–121

Robinson SK (1991) Coherent motions in the turbulent boundary layer. Annu Rev Fluid Mech 23:601–639

Rogers CB, Eaton JK (1991) The effect of small particles on fluid turbulence in a flat-plate, turbulent boundary layer in air. Phys Fluids A 3:928–937

Rouson DWI, Eaton JK (2001) On the preferential concentration of solid particles in turbulent channel flow. J Fluid Mech 428:149–169

Sato Y, Fukuichi U, Hishida K (2000) Effect of inter-particle spacing on turbulence modulation by Lagrangian PIV. Int J Heat Fluid Flow 21:554–561

Sheng J, Malkiel E, Katz J (2009) Buffer layer structures associated with extreme wall stress events in a smooth wall turbulent boundary layer. J Fluid Mech 633:17–60

Smith CR, Metzler SP (1983) The characteristics of low-speed streaks in the near-wall region of a turbulent boundary layer. J Fluid Mech 129:27–54

Sommerfeld M (2003) Analysis of collision effects for turbulent gas-particle flow in a horizontal channel: part I. Particle transport. Int J Multiphase Flow 29:675–699

Sommerfeld M, Huber N (1999) Experimental analysis and modelling of particle-wall collisions. Int J Multiphase Flow 25:1457–1489

Stern F, Muste M, Beninati L-M, Eichinger B (1999) Summary of experimental uncertainty assessment methodology with example, IIHR report. Iowa institute of Hydraulic Research, The University of Iowa, Iowa City, IA

Sumer BM, Deigaard R (1981) Particle motions near the bottom in turbulent flow in an open channel. Part 2. J Fluid Mech 109: 311–337

Sumer BM, Oguz B (1978) Particle motions near the bottom in turbulent flow in an open channel. J Fluid Mech 86:109–127

Sun TY, Faeth GM (1986) Structure of turbulent bubbly jets–I. Methods and centerline properties. Int J Multiphase Flow 12:99–114

Tanière A, Oesterlé B, Monnier JC (1997) On the behaviour of solid particles in a horizontal boundary layer with turbulence and saltation effects. Exp Fluids 23:463–471

Tsuei L, Savaş Ö (2000) Treatment of interfaces in particle image velocimetry. Exp Fluids 29:203–214

Tsuji Y, Morikawa Y (1982) LDV measurements of an air-solid two-phase flow in a horizontal pipe. J Fluid Mech 120:385–409

Tsuji Y, Morikawa Y, Shiomi H (1984) LDV measurements of an air-solid two-phase flow in a vertical pipe. J Fluid Mech 139: 417–434

Wallace JM (2009) Twenty years of experimental and direct numerical simulation access to the velocity gradient tensor: what have we learned about turbulence? Phys Fluids 21:021301–021317

Willmarth WW, Lu SS (1972) Structure of the Reynolds stress near the wall. J Fluid Mech 55:65–92

Wu Y, Christensen KT (2006) Population trends of spanwise vortices in wall turbulence. J Fluid Mech 568:55–76

Wu Y, Wang H, Liu Z, Li J, Zhang L, Zheng C (2006) Experimental investigation on turbulence modification in a horizontal channel flow at relatively low mass loadings. Acta Mech Sinica 22:99–108